



Rational design of porous Ni-Co-Fe ternary metal phosphides nanobricks as bifunctional electrocatalysts for efficient overall water splitting

Ang Li, Ling Zhang, Fangzheng Wang, Li Zhang, Li Li, Hongmei Chen^{*}, Zidong Wei^{*}

The State Key Laboratory of Power Transmission Equipment & System Security and New Technology, Chongqing Key Laboratory of Chemical Process for Clean Energy and Resource Utilization, College of Chemistry and Chemical Engineering, Chongqing University, Chongqing 400044, China

ARTICLE INFO

Keywords:

Bifunctional catalysis
Large current density
Overall water splitting
Density functional theory

ABSTRACT

Precise control is critically significant for synthesizing highly efficient bifunctional water splitting electrocatalyst. This study has developed a facile strategy for fabricating porous Ni-Co-Fe ternary metal phosphides nanobricks (denoted as Ni-Co-Fe-P NBs) with specified components and morphology. The optimized sample of Ni-Co-Fe-P NBs showed remarkable electrocatalytic performance in 1.0 M KOH. When served as bifunctional electrocatalyst for overall water splitting, the Ni-Co-Fe-P NBs required a low cell voltage of 1.46 V to achieve a current density of 10 mA cm⁻² along with superior durability. Density functional theory (DFT) calculation revealed that the homogeneously distributed Ni and Fe can optimize ΔG_{H^+} , and therefore enhance their HER activity. In the case of OER, introducing Ni, Fe and P can promote the formation of desired Co⁴⁺ sites and stabilize O-containing intermediates (H*, OH*, OOH*) on the surface of the catalysts.

1. Introduction

As an advanced technology for producing clean and sustainable hydrogen energy, electrochemical water splitting has received increasing research interests [1,2]. However, the state-of-the-art electrocatalysts for water splitting are generally precious metal-based materials (Pt/C for HER and RuO₂/IrO₂ for OER) due to the kinetically sluggish electrode reactions [3,4]. Owing to the extravagant price and low stability, these electrocatalysts are inapplicable to the industrial-level water splitting. To develop highly active, stable and earth-abundant alternatives, numerous types of nonprecious metal-based materials have been researched as bifunctional electrocatalysts for water splitting, such as single-atom catalysts [5,6], transition metal oxides [7,8], hydroxides [9,10], sulphides [11,12], nitrides [13,14], selenides [15,16], and phosphides [17,18].

Recently, transition metal phosphides (TMPs) have caught much more attention because of their impressive activity, stability, and electrical conductivity [19–21]. To boost the intrinsic activity, what generally done is to introduce heteroatoms into the host materials to modulate the electronic structure [22–24]. For example, a P-doped Ni-Mo bimetal aerogel (Ni-Mo-P) catalyst showed impressively low overpotential of 69 mV for HER, at a current density of 10 mA cm⁻² in 1.0 M KOH due to the electron regulation by Mo and P doping. DFT

calculations showed that the ΔG_{H^+} for Ni-Mo-P was -0.12 eV, better than those for Ni-Mo (-0.15 eV) and Ni (-0.39 eV), and much closer to the optimum value of zero [25]. Besides, a Ru-doped three-dimensional flower-like bimetallic phosphide on nickel foam (Ru-NiCoP/NF) effectively drove both OER (216 mV @ 20 mA cm⁻²) and HER (44 mV @ 10 mA cm⁻²) in 1 M KOH [26]. The ΔG_{H^+} value of Ru-NiCoP-Ni was very close to zero, -0.034 eV. Meanwhile, Ru-NiCoP-Ni has a lower theoretical overpotential of 0.56 V than NiCoP-Ni (1.89 V), which meant the replacement of Ni by Ru in NiCoP could promote OER. Apart from enhancing the intrinsic activity, making more active sites accessible is also of great significance [27,28]. To this end, constructing porous and/or hollow structure directly on an electroconductive substrate is one of the preferred strategies [29,30]. The hollow porous Mo-doped CoP required overpotentials of only 40 and 305 mV to drive a current of 10 mA cm⁻² for HER and OER, respectively [31]. The Mo₃P/Mo nanobelts with porous structure exhibited a small overpotential of 78 mV at a current density of 10 mA cm⁻² and a low Tafel slope of 43 mV dec⁻¹, as well as long-term stability in alkaline media, surpassing the Pt wire [32]. However, in terms of industrial application, especially at large current density (> 500 mA cm⁻²), the TMPs still leave much to be desired due to the difficulty in precise control of dopants as well as thorough exposure of active sites [33,34]. According to DFT calculations, we found that the adsorption of

^{*} Corresponding authors.

E-mail addresses: chenhongmei926@163.com (H. Chen), zdwei@cqu.edu.cn (Z. Wei).

<https://doi.org/10.1016/j.apcatb.2022.121353>

Received 9 January 2022; Received in revised form 7 March 2022; Accepted 24 March 2022

Available online 28 March 2022

0926-3373/© 2022 Elsevier B.V. All rights reserved.

hydrogen on Co_2P is too strong with the ΔG_{H^+} at -0.54 eV. Although doping or alloying heteroatoms is an effective method to boost the HER performance, the unavoidable formation of noninteracting two-phase structure is disadvantageous for modulating ΔG_{H^+} [35,36].

Herein, by taking advantage of metal-organic frameworks, porous Ni-Co-Fe ternary metal phosphides nanobricks (denoted as Ni-Co-Fe-P NBs) with precisely adjustable components and morphology have been prepared for catalyzing overall water splitting. The optimized Ni-Co-Fe-P NBs showed great ability for facilitating water dissociation and favorable chemisorption toward hydrogen intermediates that largely ameliorated the overpotentials (31, 112 and 190 mV @ 10, 100 and 800 mA cm^{-2}) and Tafel slope (65 mV dec^{-1}) of HER in 1.0 M KOH. The Ni-Co-Fe-P NBs furnished more active sites and smaller electron transfer resistance, thus the activity toward OER has been substantially improved, delivering OER current densities of 10, 100 and 800 mA cm^{-2} at low overpotentials respectively of 187, 221 and 262 mV and with Tafel slope of only 29 mV dec^{-1} . Furthermore, the cell potential for overall water splitting with Ni-Co-Fe-P NBs as both anode and cathode catalysts was merely 1.46 V for a current density of 10 mA cm^{-2} with good durability of about 100 h. The as-prepared Ni-Co-Fe-P NBs as bifunctional catalysts outperformed the commercial $\text{Pt/C}||\text{RuO}_2$ system, suggesting the promising potential of low-cost transition metal phosphides for alkaline water electrolysis.

2. Experimental section

2.1. Chemicals and reagents

Nickel foam was purchased from Kunshan Kuangxun Ltd. (China). Commercial Pt/C (40% wt%), RuO_2 and Nafion (5 wt%) were purchased from Sigma-Aldrich Chemical Reagent Co., Ltd., and 1,4-benzenedicarboxylic (BDC), potassium hydroxide (KOH), cobalt nitrate hexahydrate ($\text{Co}(\text{NO}_3)_2 \cdot 6\text{H}_2\text{O}$), nickel nitrate hexahydrate ($\text{Ni}(\text{NO}_3)_2 \cdot 6\text{H}_2\text{O}$), potassium ferricyanide ($\text{K}_3[\text{Fe}(\text{CN})_6]$), sodium hypophosphite ($\text{NaH}_2\text{PO}_2 \cdot \text{H}_2\text{O}$), ammonium fluoride (NH_4F) from Shanghai Titan Science & Technology Co., Ltd. All reagents were used as received. The water used throughout all experiments was deionized water.

2.2. Synthesis of NiCo-BDC NBs precursor

Firstly, the nickel foam ($5 \times 1 \text{ cm}^2$) was ultrasonic cleaning with ethanol, 3 M HCl aqueous solution, and deionized water for 20 min sequentially. Then, NiCo-BDC NBs were grown on nickel foam by a hydrothermal method (see Scheme 1). Take Ni_1Co_4 -BDC NBs as an example. Firstly, 2.1 mmol of 1,4-benzenedicarboxylic (BDC) was dissolved in 35 ml water and then, the pH of the solution was kept at alkaline (pH = 9) by addition of 1 M NaOH with vigorous magnetic stirring for 15 min, named Solution A. Secondly, 3.36 mmol of $\text{Co}(\text{NO}_3)_2 \cdot 6\text{H}_2\text{O}$, 0.84 mmol $\text{Ni}(\text{NO}_3)_2 \cdot 6\text{H}_2\text{O}$ and 8.4 mmol of NH_4F were dissolved in 35 ml water to form dark red solution, denoted as Solution B. Subsequently, Solution A was mixed with Solution B under vigorous magnetic stirring until the solution turned transparent. The solution was then transferred into a 100 ml PTFE-lined stainless steel autoclave

containing a piece of clean nickel foam ($1 \times 5 \text{ cm}$). The autoclave was sealed and heated at 140°C for 6 h and cooled naturally to room temperature by the end of the reaction. Take out the nickel foam, rinse the surface alternately with deionized water and ethanol, and dry it in a vacuum drying oven at 60°C for 12 h (denoted as Ni_1Co_4 -BDC NBs). With other experimental conditions fixed, by adjusting the molar ratios of Ni and Co in Solution B at 0:1, 1:4, 2:3, 1:1, 3:2, 4:1 and 1:0, a series of samples (Ni_xCo_y -BDC NBs, x/y stands for the molar ratio of Ni to Co) were obtained. The actual Ni/Co molar ratios in Ni_xCo_y -BDC NBs were determined by ICP-AES (see Table S1).

2.3. Synthesis of NiCoFe-PBA NBs precursor

3.5 mmol $\text{K}_3\text{Fe}(\text{CN})_6$ was dissolved in 70 ml water to form a bright yellow solution and then, transferred into a 100 ml PTFE-lined stainless steel autoclave containing a piece of Ni_1Co_4 -BDC NBs. The autoclave was sealed and heated at 150°C for 6 h and then cooled naturally to room temperature. Take out the nickel foam, rinse it alternately with deionized water and ethanol until the surface was free of impurities, and place it in a 60°C vacuum drying oven for 12 h to obtain NiCoFe-PBA NBs intermediate products. The contents of Fe in NiCoFe-PBA were tuned by changing the concentrations of $\text{K}_3\text{Fe}(\text{CN})_6$ to 1, 2, 3, 5 and 10 mM (denoted as $\text{Ni}_1\text{Co}_4\text{Fe}_z$ -PBA NBs, z stands for the concentration of $\text{K}_3\text{Fe}(\text{CN})_6$ in unit of mM).

2.4. Synthesis of Ni-Co-Fe-P NBs

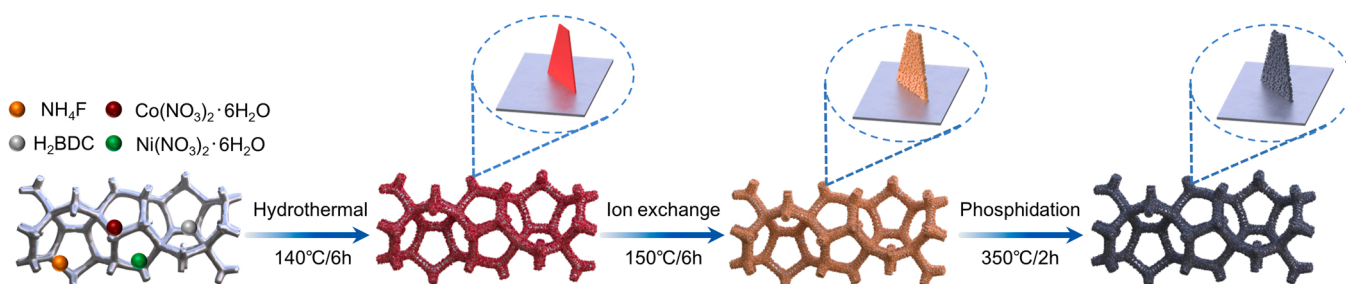
Put the obtained $\text{Ni}_1\text{Co}_4\text{Fe}_z$ -PBA NBs intermediates and 0.5 g $\text{NaH}_2\text{PO}_2 \cdot \text{H}_2\text{O}$ into two clean porcelain boats. The porcelain boat with $\text{NaH}_2\text{PO}_2 \cdot \text{H}_2\text{O}$ was then placed at the upstream of the tube furnace (near the inlet end), and the other containing NiCoFe-PBA NBs intermediates at the downstream (near the outlet end). The furnace was heated to 350°C at a heating rate of 5°C min^{-1} and maintained for 2 h in N_2 atmosphere (55 sccm). Then the reaction system was cooled naturally down to room temperature in the furnace to obtain the final Ni-Co-Fe-P NBs (denoted as $\text{Ni}_1\text{-Co}_4\text{-Fe}_z\text{-P NBs}$).

2.5. Synthesis of CoP NBs and Ni-Co-P NBs

The phosphating reaction process were performed in similar procedures by replacing the NiCoFe-PBA NBs with Co-BDC NBs and Ni_1Co_4 -BDC NBs.

2.6. Material characterization

Powder X-ray diffraction (PXRD) data were obtained using a PANalytical X'pert diffractometer with $\text{Cu K}\alpha$ radiation ($\lambda = 1.5418 \text{ \AA}$). The morphology and chemistry of the samples were characterized by a field emission scanning electron microscopy (FE-SEM) (model JSM-7600 F, JEOL Ltd., Tokyo, Japan). Transmission electron microscopy (TEM) measurements were performed on a HITACHI H-8100 electron microscopy (Hitachi, Tokyo, Japan) with an accelerating voltage of 200 kV. The energy dispersive X-ray (EDX) mapping was carried out to detect the



Scheme 1. Schematic illustration of the preparation of hierarchically porous Ni-Co-Fe-P NBs.

element composition and distribution in Ni-Co-Fe-P NBs. The functional groups present in the synthesized materials were investigated by employing a BRUKER Optik GmbH model TENSOR 27 FT-IR spectrometer. X-ray photoelectron spectroscopy (XPS) measurements were conducted by using a Thermo ESCALAB 250Xi with an Al K α (1486.6 eV) X-ray source on the samples with binding energies referenced to adventitious carbon at 284.8 eV. The specific surface areas of samples were estimated by Brunauer-Emmett-Teller (BET) method. The desorption branch of isotherms was used to calculate pore size distribution by Barrett-Joyner-Halenda (BJH) method. Inductively coupled plasma atomic emission spectrometry (ICP-AES) analysis was performed on ThermoScientific iCAP 6300 Duo.

2.7. Electrochemical measurement

The three-electrode test system and Autolab (AUT72703) electrochemical workstation were employed to test the electrochemical performance of the electrodes of interest. Working electrode: 1.0 \times 1.0 cm CoP NBs, Ni₁-Co₄-P NBs and Ni₁-Co₄-Fe₂-P NBs (z = 1, 2, 3, 5, 10), commercial Pt/C (40 wt%) and RuO₂ on nickel foam were individually used as the working electrodes, a Hg/HgO electrode (1 M KOH) as the reference electrode, and a graphite plate as the counter electrode. The geometric surface area of the working electrode is 1.0 \times 1.0 cm². The Hg/HgO reference electrode was calibrated with respect to RHE according to the previous study: in 1.0 M KOH, $E_{RHE} = E_{Hg/HgO} + 0.0591 \text{ pH} + 0.098$. Before the hydrogen evolution activity test, the cyclic voltammetry (CV) test was first performed in a potential range of 0.1 V to -0.4 V, with a sweeping speed of 50 mV/s and a duration of 30 cycles. After the electrode was stable, set the scanning speed to 1 mV/s and the potential range to 0.1 V to -0.9 V in 1 M KOH to obtain the linear voltammetry (LSV) curve; during the oxygen evolution activity test, the scanning parameters of the cyclic voltammetry (CV) were set as follows: the potential interval was 1.2–1.6 V (vs. RHE), and the scanning speed was 50 mV/s for 30 cycles. After the electrode was stable, the scanning speed was reset at 1 mV/s for linearization. During the linear Voltammetry scan (LSV), the potential range was set to 2–1.0 V (vs. RHE). Electric double layer capacitance test: For the HER reaction, cyclic voltammetry (CV) was used, and the potential range was 0.93–1.03 V (vs. RHE); the scanning speed was 5–23 mV/s; in the case of OER reaction, the cycle was also Voltammetry scan (CV), the potential range was 1.0–1.1 V (vs. RHE); the scanning speed was 5–50 mV/s. The overall water splitting performance was assessed in a two-electrode system, where the optimized Ni-Co-Fe-P NBs were chosen as anode and cathode. Electrochemical impedance test: Use the AC impedance method to measure the solution resistance and charge transfer resistance of the reaction system. The high and low frequency range was 10⁵–0.01 Hz, the bias applied in the HER reaction was -0.1 V (vs. RHE), and the overpotential measured in the OER reaction was 0.56 V (vs. RHE). Stability test: Use chronopotentiometry to evaluate the stability of hydrogen evolution electrode materials. In the constant current tests of hydrogen evolution reaction, oxygen evolution reaction and overall water splitting, the current densities were set at 20 and 100 mA cm⁻².

2.8. DFT calculations

All spin-polarized density functional theory (DFT) calculations were performed by utilizing the Vienna Ab-Initio Simulation Package (VASP) code¹. The projector augmented wave (PAW) method was used to describe the ionic cores. And the electron exchange-correlation was modelled by Perdew-Burke-Ernzerhof (PBE) function within generalized gradient approximation (GGA). A cutoff energy of 500 eV was adopted for the plane-wave basis set. The convergence criterion was 10⁻⁶ eV for energy and 0.01 eV/Å for force. The Monkhorst-Pack k-point mesh was set to be 9 \times 9 \times 1 for unit cell and 3 \times 3 \times 1 for super cell. Six atomic layers slab model with (2 \times 2) unit cell was employed to simulate the

Co₂P (001) and Co(OH)₂ (01 $\bar{1}$ 2) surface. To separate adjacent periodic images, a 18 Å thick vacuum along the vertical direction was added. In all the structure optimization calculations, the bottom three layers were fixed while other atoms were fully relaxed.

As a good descriptor for HER activity, the H adsorption free energy change (ΔG_{H^*}) is calculated using the equation:

$$\Delta G_{H^*} = \Delta E_{H^*} + \Delta ZPE - T\Delta S_{H^*} \quad (1)$$

Here ΔE_{H^*} is H adsorption energy and calculated by:

$$\Delta E_{H^*} = E_{H^*+Sur} - E_{Sur} - \frac{1}{2}E_{H_2} \quad (2)$$

ZPE is zero-point energy, which could be derived from frequency by:

$$ZPE = \frac{1}{2} \sum \hbar \nu_i \quad (3)$$

Further, ΔS_{H^*} can be regarded as $\Delta S_{H^*} \cong \frac{1}{2}S_{H_2}$, where S_{H_2} is the entropy of H₂ in the gas phase at 300 K. TS and ZPE values of H₂ are from previous report.

The free energy is calculated using the equation:

$$G = E + ZPE - TS \quad (4)$$

where G , E , ZPE and TS are the free energy, total energy from DFT calculations, zero-point energy and entropic contributions (T is set to be 300 K), respectively.

TS and ZPE values of and H₂ are from previous report. And the TS , the entropic contribution value (T is set to be 300 K) of adsorbed species, is calculated after obtaining the vibrational frequencies:

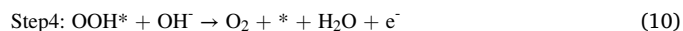
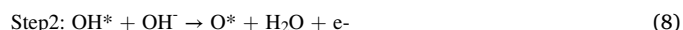
$$TS = k_B T \left[\sum \ln \left(\frac{1}{1 - e^{-\hbar \nu_i / k_B T}} \right) + \sum \frac{\hbar \nu_i}{k_B T} \left(\frac{1}{e^{\hbar \nu_i / k_B T} - 1} \right) + 1 \right] \quad (5)$$

As for the OER reaction, the adsorption free energy for adsorbed species in OER, including OH*, O* and OOH*, can be expressed by the following equation:

$$\Delta G_{ads} = \Delta E_{ads} + \Delta E_{ZPE} - T\Delta S \quad (6)$$

Where ΔE_{ads} is the adsorption energy change of adsorbates, E_{ZPE} is the zero-energy calculated from the vibrational frequencies, ΔS is the entropy change, and T is the system temperature (298.15 K, in our work).

Generally, in alkaline media, the OER reaction mechanism can be written as 4- electron change mechanism:



Where $*$ presents an adsorption site on the catalyst, and OH*, O*, and OOH* denote the corresponding adsorbed intermediates. Accordingly, the free energies of reactions (1)–(4) can be calculated using the following equations:

$$\Delta G_1 = G(\text{OH}^*) - G(*) - G(\text{OH}^-) \quad (11)$$

$$\Delta G_2 = G(\text{O}^*) + G(\text{H}_2\text{O}) - G(\text{OH}^*) - G(\text{OH}^-) \quad (12)$$

$$\Delta G_3 = \Delta G(\text{OOH}^*) - G(\text{O}^*) - G(\text{OH}^-) \quad (13)$$

$$\Delta G_4 = 4.92 - \Delta G_1 - \Delta G_2 - \Delta G_3 \quad (14)$$

The ΔG for intermediates of each step is considered as a reasonable description for the difficulty of OER. The theoretical overpotential η for OER can be calculated using the equations: $G_{\text{OER}} = \max \{ \Delta G_1, \Delta G_2, \Delta G_3, \Delta G_4 \}$, $\eta_{\text{OER}} = G_{\text{OER}}/e - 1.23 \text{ V}$.

Besides, the Gibbs energy of formation (ΔG_f) for cobalt hydroxide is $\Delta G_f(\text{CoO}_x\text{H}_y) = E(\text{CoO}_x\text{H}_y) - E_{\text{Co}} - xE_{\text{O}} - yE_{\text{H}}$.

The change in Gibbs energy for the oxidation of Ni is calculated using the following equations:

$$\Delta G(\text{Co}^{2+} \rightarrow \text{Co}^{3+}) = \Delta G_f(\text{CoOOH}) - [\Delta G_f(\text{Co}(\text{OH})_2) + \mu\text{H}] \quad (15)$$

$$\Delta G(\text{Co}^{3+} \rightarrow \text{Co}^{4+}) = \Delta G_f(\text{CoO}_2) - [\Delta G_f(\text{CoOOH}) + \mu\text{H}] \quad (16)$$

3. Results and discussion

3.1. Catalysts synthesis and characterization

The synthetic procedure of porous Ni-Co-Fe-P NBs is schematically illustrated in Scheme 1. The NiCo bimetal organic framework precursors (denoted as NiCo-BDC NBs) were first prepared by a one-pot hydrothermal reaction (see details in the Experimental section). By varying the dosages of Ni and Co precursors, the NiCo-BDC NBs with different Ni/Co ratios (signified as $\text{Ni}_x\text{Co}_y\text{-BDC NBs}$, x/y stands for the integral molar ratio of Ni to Co) were obtained. The scanning electron microscopy (SEM), X-ray diffraction (XRD) patterns, Fourier transform infrared spectroscopy (FTIR), and N_2 adsorption-desorption curves have been collected to monitor their crystal and morphology changes. The SEM images manifested that the $\text{Ni}_x\text{Co}_y\text{-BDC NBs}$ (Fig. 1b, c) took on similar triangular plate morphology with width of around 5 μm and height of around 10 μm . Furthermore, the XRD patterns (Fig. S2a) of $\text{Ni}_x\text{Co}_y\text{-BDC NBs}$ were also identical and consistent with the simulated results of $\text{Co}_2(\text{OH})_2(\text{BDC})$ (no. 985792, space group of $\text{C}_{2/m}$, Cambridge Crystallographic Data Centre), meaning they were isostructural with similar crystal structure [37]. Based on these, we came to the conclusion that each Ni and Co atom in $\text{Ni}_x\text{Co}_y\text{-BDC NBs}$ was octahedrally coordinated with six O atoms, and these octahedra were further connected at edges or corners along the [010]/[001] direction in the (200) crystallographic plane to form 2D bimetal layers separated by BDC molecules [38]. The actual Ni/Co ratios of $\text{Ni}_x\text{Co}_y\text{-BDC NBs}$ measured by ICP-AES were close to the feeding ratios (Table S1), indicating the marvelous controllability of chemical components in $\text{Ni}_x\text{Co}_y\text{-BDC NBs}$. The FT-IR spectra (Fig. S2c) confirmed the stretching vibrations of OH-, -COO- and para-aromatic CH groups in $\text{Ni}_x\text{Co}_y\text{-BDC NBs}$. The difference value (213 cm^{-1}) between the bands of $\nu_{\text{as}}(\text{-COO-})$ at 1587 cm^{-1} and $\nu_{\text{s}}(\text{-COO-})$ at 1386 cm^{-1} was indicative of the bridging nature of -COO- groups [39].

Subsequently, the $\text{Ni}_x\text{Co}_y\text{-BDC NBs}$ precursors were transformed into porous NiCo prussian blue (denoted as NiCoFe-PBA NBs) via ion

exchange reaction in $\text{K}_3\text{Fe}(\text{CN})_6$ solution. Compared to the $\text{Ni}_x\text{Co}_y\text{-BDC NBs}$ precursors, the surface of NiCoFe-PBA NBs was roughened by many nanocubes sized $\sim 200\text{ nm}$ (Fig. 1g, h). Besides, the XRD patterns showed that the intensity of diffraction peaks belonging to $\text{Ni}_x\text{Co}_y\text{-BDC NBs}$ precursors declined and those new diffraction peaks were attributed to $\text{Ni}_3[\text{Fe}(\text{CN})_6]_2$ (JCPDS card no. 20-0915) and $\text{Co}_3[\text{Fe}(\text{CN})_6]_2$ (JCPDS card no. 31-1000), respectively [40] (Fig. S2b). The FTIR (Fig. S2c) showed two absorption bands in the region of $2000\text{--}2200\text{ cm}^{-1}$, which were ascribed to the characteristic stretching vibrations of CN group. The absorption bands at 2108 cm^{-1} and 2165 cm^{-1} were assigned to the bridging cyanide and terminal cyanide groups, respectively [41]. After phosphidation of the NiCoFe-PBA precursor at 350°C , the characteristic peaks of CN were much weaker, indicating that most of NiCoFe-PBA precursor has decomposed into metallic phosphides, and only a small amount of CN existed in the metallic phosphide composite.

Furthermore, samples of NiCoFe-PBA NBs have been collected at different reaction times (denoted as NiCoFe-PBA-t, t stands for the reaction hours) to follow the structure evolution. Unlike the smooth-surfaced $\text{Ni}_x\text{Co}_y\text{-BDC NBs}$ precursors, nanocubes were spotted on NiCoFe-PBA-t. When prolonging the reaction time, the NiCoFe-PBA-t turned progressively to porous structure (Fig. S1a-f). The intensity of XRD patterns for NiCoFe-PBA-t declined gradually with extending reaction time, implying dissociation of the precursors (Fig. S2b). Owing to the relatively weak bonds between metal ions and organic ligands in NiCo-BDC NBs, the internal Ni and Co dissociated slowly to develop inner voids. What is more, the liberated Ni and Co ions combined with the $\text{Fe}(\text{CN})_6^{3-}$ ions to form $\text{Ni}_3[\text{Fe}(\text{CN})_6]_2$ and $\text{Co}_3[\text{Fe}(\text{CN})_6]_2$ nanocubes to roughen the surface.

The final porous Ni-Co-Fe-P NBs were obtained by phosphidating the NiCoFe-PBA precursors in a quartz tube furnace at specified temperatures. All the diffraction peaks of Ni-Co-Fe-P NBs (XRD, Fig. 1f) were well indexed to the Co_2P phase (JCPDS card: 54-0413) with no peaks of Fe_3P and Ni_3P detected, indicating both Ni and Fe have been introduced into Co_2P matrix through isomorphous substitution. Fig. S2d revealed that the Ni-Co-Fe-P NBs samples in different iron contents have similar crystal structure. Furthermore, Fig. S3b and Table S2 demonstrated the linear relationship between the actual molar ratios of Fe to the total metals in Ni-Co-Fe-P NBs and the concentrations of $\text{K}_3\text{Fe}(\text{CN})_4$, signifying the Fe contents in Ni-Co-Fe-P NBs could also be readily modulated. Combining the SEM images and ICP results, we concluded that this two-step synthesis strategy realized precise control over the chemical components and morphology of the Ni-Co-Fe ternary metal phosphides.

Scanning transmission electron microscopy (STEM, Fig. 1i) further

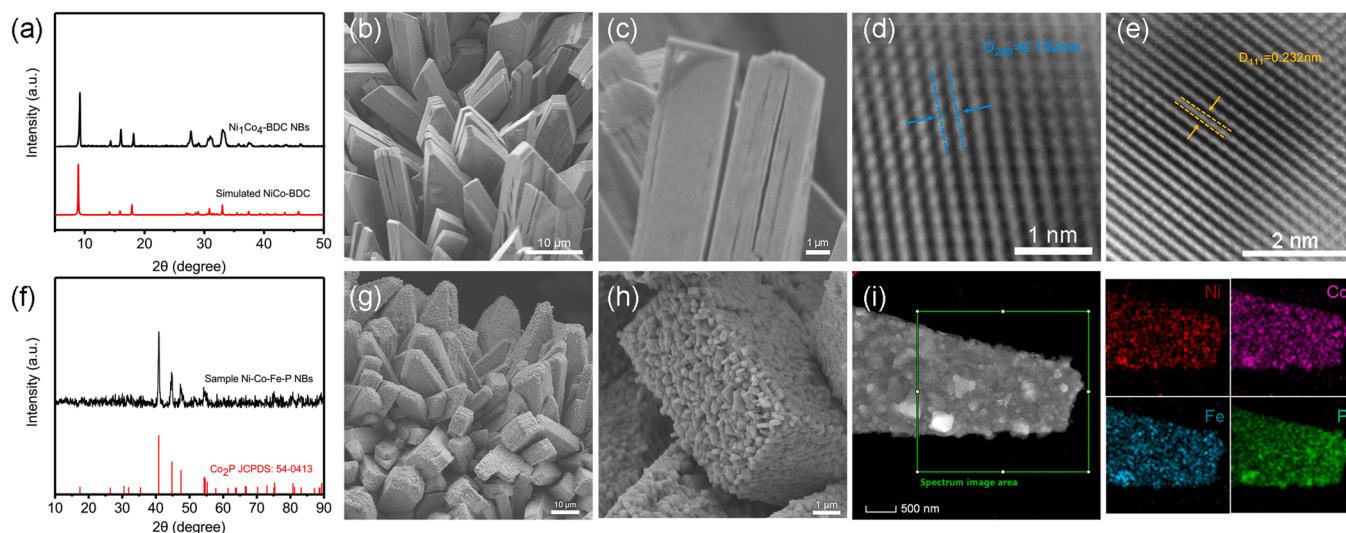


Fig. 1. XRD patterns of synthesized $\text{Ni}_1\text{Co}_4\text{-BDC NBs}$ (a) and Ni-Co-Fe-P NBs (f), SEM images of NiCo-BDC arrays (b, c) and Ni-Co-Fe-P NBs (g, h), HRTEM images of NiCo-BDC NBs (d, e), low-magnification STEM HAADF image of Ni-Co-Fe-P NBs (i), and the corresponding elemental mapping.

revealed the presence of nanoparticles sized 100–200 nm on the surface of Ni-Co-Fe-P NBs. The high-resolution TEM images (HRTEM, Fig. 1d, e) displayed well-resolved lattice fringes with interplanar distances of 1.92 and 2.23 Å, corresponding to the (200) and (111) lattice planes of Co_2P (JCPDS 54–0413). The energy dispersive X-ray (EDX) mapping shed light on the homogeneous distribution of Co, Ni, Fe, and P in Ni-Co-Fe-P NBs. During the second hydrothermal reaction between the simultaneously released metal and $\text{Fe}(\text{CN})_6^{3-}$ ions, small pores formed on the surface of NiCo-MOFs [21,34]. The Brunauer-Emmett-Teller (BET) curve (Fig. S4) showed that the specific surface area of Ni-Co-Fe-P NBs reached $185.461 \text{ m}^2 \text{ g}^{-1}$, 180 times larger than that of Ni-Co-P ($1.218 \text{ m}^2 \text{ g}^{-1}$), highlighting the remarkable effect of iron on the final porous structure.

The chemical states of Co-P NBs, Ni-Co-P NBs and Ni-Co-Fe-P NBs were explored with X-ray photoelectron spectroscopy (XPS) (Fig. 2). The overall spectrum of Ni-Co-Fe-P NBs (Fig. 2a) manifested the coexistence of Co, Ni, Fe, and P without any detectable impurity. The corresponding high-resolution Co 2p spectrum (Fig. 2b) was deconvoluted into three spin-orbit doublets, of which peaks at 781.8/799.2 eV and 779.2/794.1 eV were assigned to the Co^{2+} ($0 < \delta < 2$) species bonded to P and Co^{2+} , respectively. The doublets at 786/803.5 eV were ascribed to the shakeup satellite peaks. The Ni 2p in Ni-Co-Fe-P NBs (Fig. 2c) was deconvoluted into three doublets. The doublets at 853.7/870.8 eV were assigned to Ni^{2+} species bonded to P, whereas doublets at 856.7/875.2 eV and 862.2/880.3 eV accounted for the Ni^{2+} species and shakeup satellite peaks, respectively. It should be noted that the presence of Ni^{2+} and Co^{2+} resulted from the unavoidable surface oxidation by air. Compared to the Co 2p and Ni 2p spectra in Ni-Co-P NBs (Fig. 2b, c), the binding energy of Co and Ni in Ni-Co-Fe-P NBs shifted positively by 0.4 eV and 0.2 eV, showing the electronic structure of Ni and Co in Ni-Co-P NBs had been modified by Fe doping. Deconvolution of the peaks of Fe 2p spectrum (Fig. S11f) resulted in three spin-orbit doublets

located at 711/713.8 eV and 716.7/725.8 eV, which were ascribed to the Fe bonded to P ($\text{Fe}^{\delta+}$, $0 < \delta < 2$) and Fe^{2+} and the shakeup satellite peak, respectively. The P 2p spectra (Fig. 3d) in Ni-Co-Fe-P NBs represented the P $2p_{3/2}$ (129.4 eV), P $2p_{1/2}$ (130.4 eV) and P-O species (133.9 eV) on the surface. Meanwhile, the binding energies of P (2p) shifted positively, indicative of the strong interaction between P and the metal atoms. The results of XPS technique proved that concurrence of Ni and Fe cations in Ni-Co-Fe-P NBs effectuated not only the increased specific surface area but also the formation of high-valent Co sites.

3.2. Hydrogen evolution reaction measurement

The HER activities of Ni-Co-Fe-P NBs, Co-P NBs, Ni-Co-P NBs, and Pt/C (40%) of same mass loading (ca. 4 mg cm^{-2}) were first evaluated using a three-electrode configuration in 1 M KOH saturated by H_2 . A slow scanning speed (1 mV/s) was adopted to minimize the background currents, and all the potentials were corrected with reference to the reversible hydrogen electrode (RHE). By the polarization curves (Fig. 3a), the Ni-Co-Fe-P NBs required an overpotential of 32 mV to yield a current density of 10 mA cm^{-2} , larger than that of Pt/C (19 mV), but substantially lower than those of Ni-Co-P NBs (63 mV) and Co-P NBs (92 mV); however, the overpotentials of Ni-Co-Fe-P NBs at current densities of 100 and 800 mA cm^{-2} were encouragingly the lowest, only 112 mV and 190 mV, respectively.

To understand the HER process, the Tafel plot analysis (Fig. S5b) were also performed, and the Ni-Co-Fe-P NBs exhibited a Tafel slope of 65 mV dec^{-1} , smaller than those of Ni-Co-P NBs and Co-P NBs (85 and 112 mV dec^{-1} , respectively). The Tafel slope revealed that, under the specified conditions, the HER catalyzed by Ni-Co-Fe-P NBs proceeded via the Volmer–Heyrovsky mechanism, i.e., the electrochemical desorption of hydrogen was the rate-determining step. Furthermore, the Ni-Co-Fe-P NBs also outperformed most previously reported

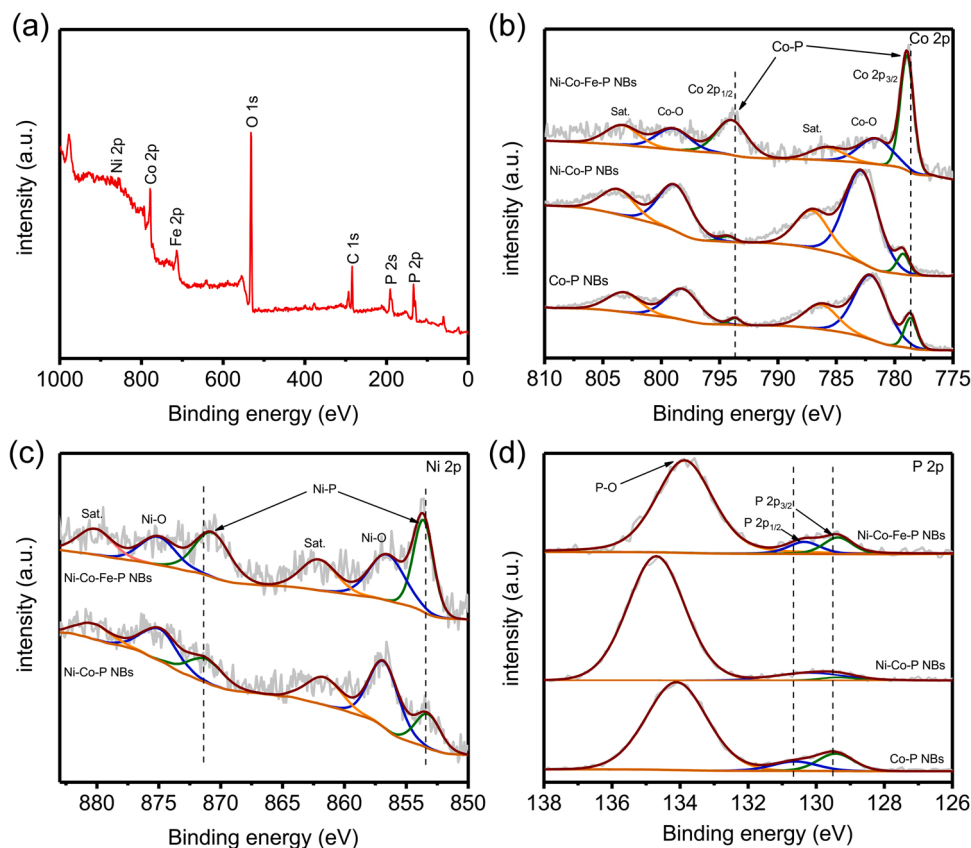


Fig. 2. (a) XPS survey spectrum of Ni-Co-Fe-P NBs, (b) High resolution XPS spectra of Co 2p and (d) Ni 2p of Ni-Co-P NBs and Ni-Co-Fe-P NBs, (e) P 2p of Co-P NBs, Ni-Co-P NBs and Ni-Co-Fe-P NBs.

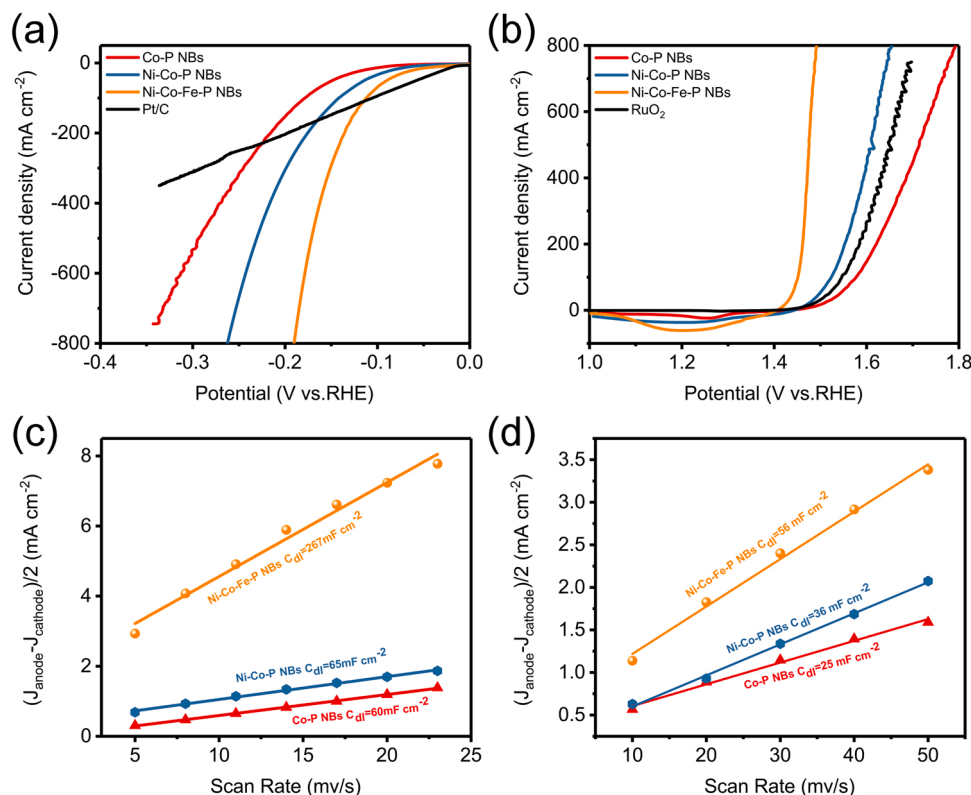


Fig. 3. (a) Polarization curves of Co-P NBs, Ni-Co-P NBs, Ni-Co-Fe-P NBs and 40% Pt/C electrodes for HER, (b) Polarization curve of the obtained Co-P NBs, Ni-Co-P NBs, Ni-Co-Fe-P NBs and RuO₂ electrodes for OER, (c) the corresponding double-layer capacitances for HER, (d) the corresponding double-layer capacitances for OER. All results shown were corrected by iR compensation, LSV scan rate: 1 mV/s.

nonprecious HER catalysts in alkaline electrolyte (Table S3). Electrochemical impedance spectroscopy (EIS) measurements (Fig. S5a) showed that the solution resistances (R_s) of all samples were similar while their charge transfer resistances (R_{ct}) varied significantly. As illustrated in the LSV curves (Fig. 3a), the R_{ct} of Ni-Co-Fe-P NBs electrode was smaller than other samples, indicating a significantly improved reaction kinetics in catalytic HER. The double-layer capacitances (C_{dl}) of Ni-Co-Fe-P NBs, Ni-Co-P NBs and Co-P NBs, which have a positive association with the electrochemical active surface areas (ECSA), were further obtained based on CV curves against various scan rates (Fig. S6a - c). The C_{dl} of Ni-Co-Fe-P NBs (Fig. S3c) was the largest (287 mF cm⁻²), presenting most accessible active sites.

3.3. Oxygen evolution reaction measurement

The OER activities of the samples were assessed in 1 M KOH (loading ca. 4.0 mg cm⁻²). The Ni-Co-Fe-P NBs also required small overpotentials of 187 and 221 mV to reach the current densities of 10 and 100 mA cm⁻² (Fig. 3b), respectively, even lower than those of RuO₂ on nickel substrate (232 and 316 mV, respectively). In addition, driving an industrial-scale current density of 800 mA cm⁻², the Ni-Co-Fe-P NBs required an overpotential of only 262 mV, 162 and 300 mV less than those of Ni-Co-P NBs and Co-P NBs, respectively. The samples of Ni-Co-Fe-P NBs assumed a similar Tafel slope of around 29 mV dec⁻¹ (Fig. S5d), which was much lower than those of RuO₂ on the nickel substrate (80 mV dec⁻¹) and the counterparts, Ni-Co-P NBs (56 mV dec⁻¹) and Co-P NBs (87 mV dec⁻¹). We can found that the activity toward Oxygen evolution reaction was better than most reported electrocatalysts (Table S4). The Nyquist plots (Fig. S5c) depicted that the charge transfer resistance (R_{ct}) of Ni-Co-Fe-P NBs was the minimal with respect to the counterparts, suggesting the fastest charge transfer across the electrode-electrolyte interface. CV measurements were conducted to attain the electrochemically active surface area (ECSA) at different scan

rates (10, 20, 30, 40, 50 mV/s) (Fig. S6d - f) with potentials ranging between 0.93 and 1.03 V verse RHE in 1 M KOH. The calculated C_{dl} values (Fig. 3d) of Ni-Co-Fe-P NBs, Ni-Co-P NBs and Co-P NBs were 56, 36 and 25 mF cm⁻², respectively. Besides, the amounts of O₂ and H₂ produced in an H-type electrolytic apparatus with Ni-Co-Fe-P NBs as the bifunctional electrocatalysts were measured by water drainage. As shown in Fig. S15, the water container was separated with a Nafion membrane. It is worth pointing out that 4.1 ml of O₂ and 8 ml of H₂ was generated within 25 min. The ratio of H₂ to O₂ (2:1) was consistent with the theoretically calculated value, indicative of a Faradaic efficiency of approximate 100%.

3.4. Overall water splitting measurement

Considering the impressive electrocatalytic performances of Ni-Co-Fe-P NBs toward both OER and HER, we followed up the overall water splitting performance by assembling a two-electrode cell using Ni-Co-Fe-P NBs as catalysts for both cathode and anode. Meanwhile, a water electrolyzer was constructed with commercial benchmarks (RuO₂ for OER and Pt/C for HER with the same loading mass, ca. 4 mg cm⁻², on nickel substrate) for control experiments. The LSV curves (Fig. 4c) unveiled the notable catalytic activity of Ni-Co-Fe-P NBs toward overall water splitting, requiring a small cell voltage of 1.46 V to attain a current density of 10 mA cm⁻², which is better than Pt/C/NF || RuO₂/NF (1.48 V). In the case of large current densities, it reached 800 mA cm⁻² at 1.98 V, better than Pt/C/NF || RuO₂/NF (2.72 V), indicating that it is a promising alternative for the practical application of water splitting. To our knowledge, such low cell voltage is superior to those of most previously reported overall water splitting electrocatalysts, and even better than those of noble metal-based materials (Table S5).

To appraise the long-term stability, the electrode made with Ni-Co-Fe-P NBs was first investigated via a chronoamperometric method at constant current densities of 20 and 100 mA cm⁻² for both HER and

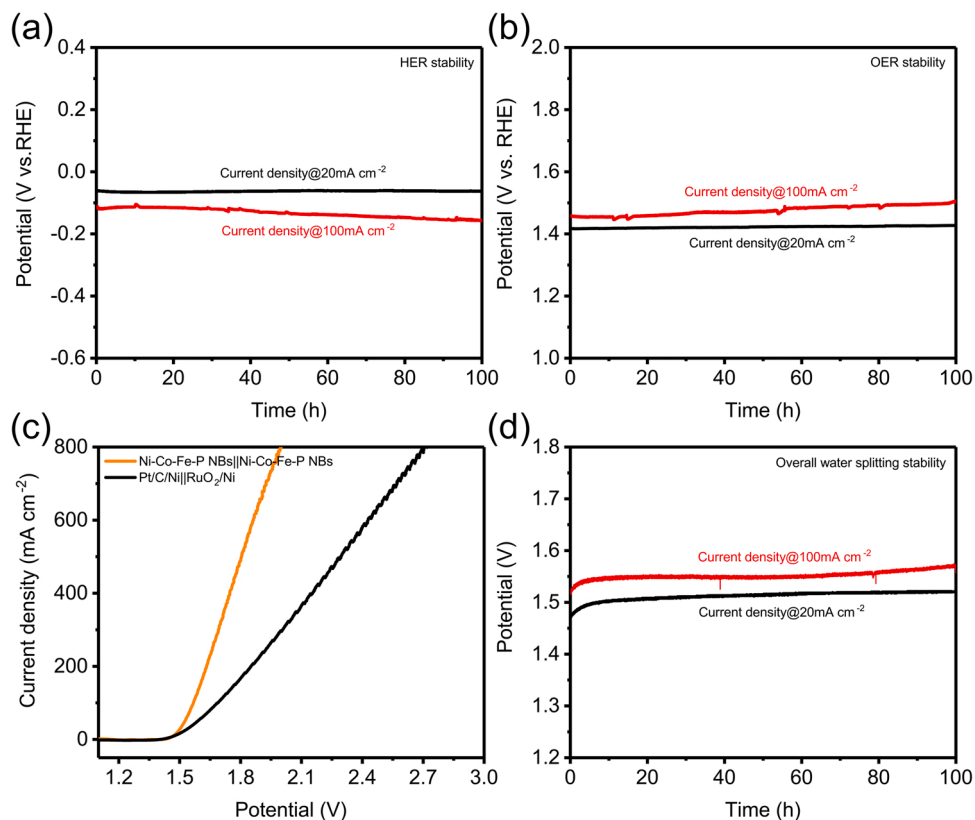


Fig. 4. Time dependence of the potentials of Ni-Co-Fe-P NBs under constant current densities of -20 and -100 mA cm⁻² for HER (a) and OER (b), (c) LSV curves of Ni-Co-Fe-P NBs (orange) as bifunctional catalysts in 1.0 M KOH solution for overall water splitting. RuO₂ and Pt/C as OER and HER benchmarks were measured for comparison (black), (d) Time dependence of the potentials of Ni-Co-Fe-P NBs for overall water splitting under constant current densities of 20 and 100 mA cm⁻².

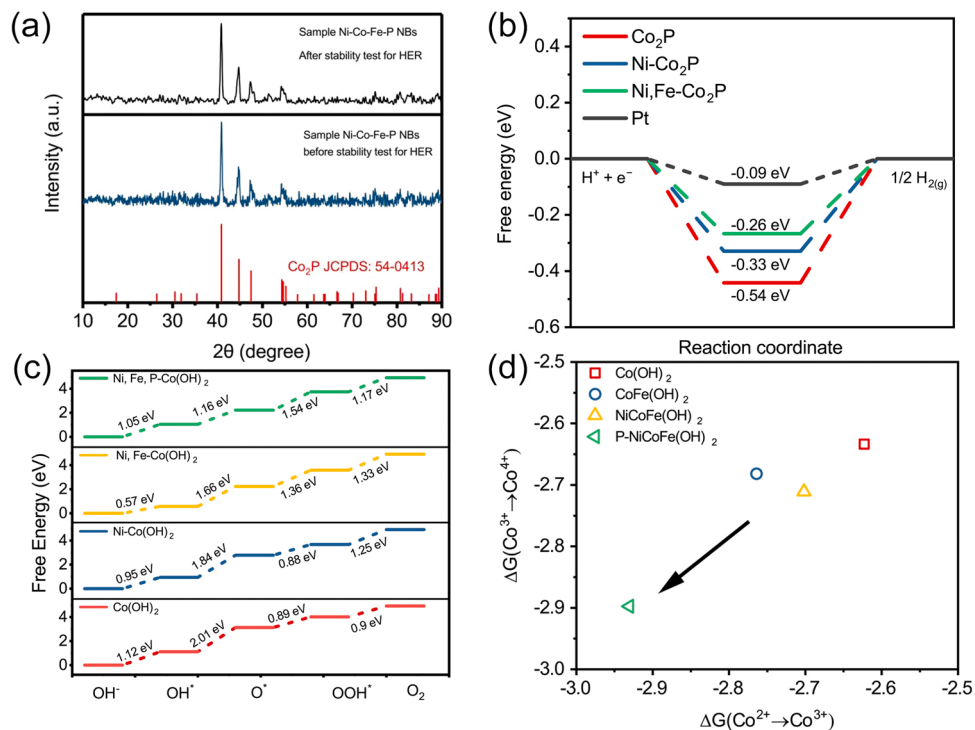


Fig. 5. (a) XRD characterization of Ni-Co-Fe-P NBs before and after stability test for HER, (b) the corresponding free energy diagram for HER on Co₂P, Ni doped Co₂P, Ni, Fe co-doped Co₂P and Pt, (c) the corresponding free energy diagram for OER on Co(OH)₂, Ni-Co(OH)₂, Ni, Fe-Co(OH)₂ and Ni, Fe, P-Co(OH)₂ at U = 0 V, and (d) DFT calculated free energies for the oxidations of Co²⁺ to Co⁴⁺ on Co(OH)₂, Ni-Co(OH)₂, Ni, Fe-Co(OH)₂ and Ni, Fe, P-Co(OH)₂.

OER over 100 h. After the tests, the overpotentials of Ni-Co-Fe-P NBs increased respectively only 12 and 50 mV for HER (Fig. 4a) and 8 and 60 mV for OER (Fig. 4b). Then, its stability as bifunctional electrocatalysts for overall water splitting under the same conditions were also assessed in a two-electrode system. The potentials increased only 22 and 30 mV after 100 h at 20 and 100 mA cm⁻² (Fig. 4d), respectively, with morphology well-retained. The excellent performance and stability of Ni-Co-Fe-P NBs are crucial and count for much in their practical application to water splitting.

3.5. Mechanism analysis

To pinpoint the origins of HER and OER activities of Ni-Co-Fe-P NBs, the XRD patterns and XPS spectra have been performed to delve into their crystal structures and chemical states. The identical XRD patterns (Fig. S1a), XPS spectra (Fig. S10) and SEM images (Fig. S11b) revealed no changes in crystal structure and chemical state during HER. Based on the XRD patterns and TEM images, Co₂P (001) has been studied theoretically by DFT (Fig. S1b). The adsorption free energy change (ΔG_H) of Co₂P (001) for hydrogen was -0.54 eV, suggesting the strong adsorption toward hydrogen. After incorporating Ni into Co₂P (001), the ΔG_H of Ni doped Co₂P (001) decreased to -0.36 eV. Furthermore, Ni, Fe co-doped Co₂P (001) further reduced the ΔG_H to a more favorable value, -0.26 eV. To investigate the effects of heteroatoms on the electronic structure of host materials, we carried out a density of states (DOS) analysis (Fig. S13a). The d-band center of Co₂P located at -1.26 eV. In contrast, the d-band centers of Ni doped Co₂P (001) and Ni, Fe co-doped Co₂P (001) shifted to -1.47 eV and -1.57 eV, respectively, revealing the fading interactions with the adsorbed hydrogen.

On the other hand, nearly no diffraction peaks in the XRD patterns of Ni-Co-Fe-P NBs after OER tests could be discerned. These observations uncovered the transformation of Ni-Co-Fe-P NBs from the original crystal structure to amorphous structure (Fig. S11a). Moreover, the XPS spectra (Fig. S11b-e) of Ni-Co-Fe-P NBs after OER tests verified that the Ni-P, Co-P and Fe-P doublets were replaced by those of Ni-O, Co-O and Fe-O, indicating the true active species for OER was Ni, Fe and P co-doped Co(OH)₂. These morphologic and structural characterizations both confirmed the fact that the catalyst surface encountered irreversible oxidation during OER. Therefore, it was safely inferred that the electrocatalysts that played roles in OER took on the form of P-doped NiCoFe(OH)₂ (denoted as Ni, Fe, P-Co(OH)₂) due to the oxidation of Ni-Co-Fe-P NBs. SEM images obtained postmortem exhibited thicker layers and rougher surfaces after long-term reaction (Fig. S12c), which possibly resulted from surface rearrangement of the catalyst during OER. The calculated free energy diagrams (Fig. 5c) revealed that the formation of OOH* intermediates was the most sluggish step for both Ni-Co-P NBs and Ni-Co-Fe-P NBs as the catalysts of OER and often considered as the rate-limiting step because of the high energy required to stabilize the OOH* intermediates. After doping Ni and Fe, the theoretical overpotential of Co(OH)₂ toward OER was lowered to 0.78 V and that of P-doped NiCoFe(OH)₂ declined to 0.31 V. The as-prepared Ni-Co-Fe-P NBs were oxidized and converted into P-NiCoFe(OH)₂, which was beneficial for the formation of high valence Co⁴⁺ ions and promotion of the sluggish OER [42,43]. It has been demonstrated that metal ions at higher valences are more beneficial to OER reaction and the lower the formation energy, the easier its formation [44–46]. In this study, the formation energy of Co⁴⁺ on the P-doped NiCoFe(OH)₂ has also been calculated (Fig. 5d). The Gibbs energies of oxidations from Co²⁺ to Co³⁺ and Co³⁺ to Co⁴⁺ in Co(OH)₂ were determined to be -2.69 eV and -2.9 eV, respectively. Fig. 5d demonstrated that successive doping Ni, Fe and P into Co(OH)₂ could lower dramatically the formation energy of Co⁴⁺, implying the high occurrence of Co⁴⁺ ions in NiCoFe(OH)₂ and thus explicating the high electroactivity of Ni-Co-Fe-P NBs toward OER.

4. Conclusion

In summary, this study revealed that the metal-organic frameworks could be employed to synthesize porous Ni-Co-Fe ternary metal phosphides nanobricks (Ni-Co-Fe-P NBs) with specified components and morphology as high-performance bifunctional electrocatalysts for practical over water splitting. The activity and stability of Ni-Co-Fe-P NBs toward both HER and OER were found to be superior to most previously reported nonprecious materials, even better than the benchmark catalysts at industrial-level current density. Therefore, the Ni-Co-Fe-P NBs hold great promise for large-scale clean H₂ production. Besides, the facile synthetic strategy herein may also be extended to acquire other high-performance bifunctional TMPs electrocatalysts for overall water splitting.

CRediT authorship contribution statement

Ang Li: Conceptualization, Writing – original draft, Methodology, Investigation. **Ling Zhang:** Data curation, DFT calculation, Formal analysis. **Fangzheng Wang:** Software. **Li Zhang:** Software. **Li Li:** DFT Calculation. **Hongmei Chen:** Data curation, Formal analysis, Funding acquisition, Project administration, Writing – review & editing, Conceptualization, Supervision. **Zidong Wei:** Data curation, Project administration, Formal analysis, Writing – review & editing.

Declaration of Competing Interest

The authors declare that they have no known competing financial interests or personal relationships that could have appeared to influence the work reported in this paper.

Acknowledgements

We gratefully acknowledge the support of this research by Ministry of Science and Technology of China (Nos. 2021YFB4000300) and the National Natural Science Foundation of China (Nos. 22075033).

Appendix A. Supporting information

Supplementary data associated with this article can be found in the online version at doi:10.1016/j.apcatb.2022.121353.

References

- [1] Z. Wu, Y. Zhao, H. Wu, Y. Gao, Z. Chen, W. Jin, J. Wang, T. Ma, L. Wang, Corrosion engineering on iron foam toward efficiently electrocatalytic overall water splitting powered by sustainable energy, *Adv. Funct. Mater.* 31 (2021) 2010437–2010444, <https://doi.org/10.1002/adfm.202010437>.
- [2] Z.Y. Yu, Y. Duan, X.Y. Feng, X. Yu, M.R. Gao, S.H. Yu, Clean and affordable hydrogen fuel from alkaline water splitting: past, recent progress, and future prospects, *Adv. Mater.* 33 (2021) 2007100–2007135, <https://doi.org/10.1002/adma.202007100>.
- [3] Y. Zhao, Y. Gao, Z. Chen, Z. Li, T. Ma, Z. Wu, L. Wang, Trifling Pt coupled with NiFe hydroxide synthesized via corrosion engineering to boost the cleavage of water molecule for alkaline water-splitting, *Appl. Catal. B Environ.* 297 (2021) 120359–120366, <https://doi.org/10.1016/j.apcatb.2021.120359>.
- [4] Q. Wang, Z. Zhang, C. Cai, M.Y. Wang, Z.L. Zhao, M.H. Li, X. Huang, S.B. Han, H. Zhou, Z.X. Feng, L. Li, J. Li, H. Xu, J.S. Francisco, M. Gu, Single iridium atom doped Ni₂P catalyst for optimal oxygen evolution, *J. Am. Chem. Soc.* 143 (2021) 13605–13615, <https://doi.org/10.1021/jacs.1c04682>.
- [5] D.W. Wang, Q. Li, C. Han, Z.C. Xing, X.R. Yang, Single-atom ruthenium based catalyst for enhanced hydrogen evolution, *Appl. Catal. B Environ.* 249 (2019) 91–97, <https://doi.org/10.1016/j.apcatb.2019.02.059>.
- [6] G.L. Hou, T. Yang, M. Li, J. Vanbuel, O.V. Lushchikova, P. Ferrari, J.M. Bakker, E. Janssens, Water splitting by C60-supported vanadium single atoms, *Angew. Chem. Int. Ed.* 60 (2021) 27095–27101, <https://doi.org/10.1002/anie.202112398>.
- [7] L.S. Peng, X.Q. Zheng, L. Li, L. Zhang, N. Yang, K. Xiong, H.M. Chen, J. Li, Z.D. Wei, Chimney effect of the interface in metal oxide/metal composite catalysts on the hydrogen evolution reaction, *Appl. Catal. B Environ.* 245 (2019) 122–129, <https://doi.org/10.1016/j.apcatb.2018.12.035>.
- [8] B. Deng, J. Liang, L. Yue, T. Li, Q. Liu, Y. Liu, S. Gao, A.A. Alshehri, K.A. Alzahrani, Y. Luo, X. Sun, CoFe-LDH nanowire arrays on graphite felt: a high-performance

- oxygen evolution electrocatalyst in alkaline media, *Chin. Chem. Lett.* (2021), <https://doi.org/10.1016/j.ccllet.2021.10.002>.
- [9] B. Geng, F. Yan, X. Zhang, Y. He, C. Zhu, S.L. Chou, X. Zhang, Y. Chen, Conductive CuCo-based bimetal organic framework for efficient hydrogen evolution, *Adv. Mater.* 33 (2021) 2106781–2106790, <https://doi.org/10.1002/adma.202106781>.
- [10] X. Zhang, F. Yan, X. Ma, C. Zhu, Y. Wang, Y. Xie, S.L. Chou, Y. Huang, Y. Chen, Regulation of morphology and electronic structure of FeCoNi layered double hydroxides for highly active and stable water oxidation catalysts, *Adv. Energy Mater.* 11 (2021) 2102141–2102152, <https://doi.org/10.1002/aenm.202102141>.
- [11] H. Su, S.J. Song, S.S. Li, Y.Q. Gao, L. Ge, W.Y. Song, T.Y. Ma, J. Liu, High-valent bimetal Ni₃S₂/Co₃S₄ induced by Cu doping for bifunctional electrocatalytic water splitting, *Appl. Catal. B Environ.* 293 (2021) 120225–120236, <https://doi.org/10.1016/j.apcatb.2021.120225>.
- [12] Y. Wu, Y. Li, M. Yuan, H. Hao, X. San, Z. Lv, L. Xu, B. Wei, Operando capturing of surface self-reconstruction of Ni₃S₂/FeNi₂S₄ hybrid nanosheet array for overall water splitting, *Chem. Eng. J.* 427 (2022) 131944–131955, <https://doi.org/10.1016/j.cej.2021.131944>.
- [13] C. Zhu, Z. Yin, W. Lai, Y. Sun, L. Liu, X. Zhang, Y. Chen, S.-L. Chou, Fe-Ni-Mo nitride porous nanotubes for full water splitting and Zn-air batteries, *Adv. Energy Mater.* 8 (2018) 1802327–1802339, <https://doi.org/10.1002/aenm.201802327>.
- [14] Y. Wang, Y. Sun, F. Yan, C. Zhu, P. Gao, X. Zhang, Y. Chen, Self-supported NiMo-based nanowire arrays as bifunctional electrocatalysts for full water splitting, *J. Mater. Chem. A* 6 (2018) 8479–8487, <https://doi.org/10.1039/c8ta00517f>.
- [15] H. Li, J. Liang, T. Li, L. Yue, Q. Liu, Y. Luo, M.S. Hamdy, Y. Sun, X. Sun, Recent advances in MoS₂-based materials for electrocatalysis *Chem. Comm.* (2022) <https://doi.org/10.1039/d1cc04004a>.
- [16] J.-Y. Zhang, Y. Yan, B. Mei, R. Qi, T. He, Z. Wang, W. Fang, S. Zaman, Y. Su, S. Ding, B.Y. Xia, Local spin-state tuning of cobalt–iron selenide nanoframes for the boosted oxygen evolution, *Energy Environ. Sci.* 14 (2021) 365–373, <https://doi.org/10.1039/d0ee03500a>.
- [17] J. Deng, S. Chen, N. Yao, Q. Wang, J. Li, Z.D. Wei, Integrating H₂ generation with sewage disposal by an efficient anti-poisoning bifunctional electrocatalyst, *Appl. Catal. B Environ.* 277 (2020), <https://doi.org/10.1016/j.apcatb.2020.119175>.
- [18] M.T. Jin, X. Zhang, R. Shi, Q. Lian, S.Z. Niu, O.W. Peng, Q. Wang, C. Cheng, Hierarchical CoP@Ni₂P catalysts for pH-universal hydrogen evolution at high current density, *Appl. Catal. B Environ.* 296 (2021) 120350–120360, <https://doi.org/10.1016/j.apcatb.2021.120350>.
- [19] Y. Ren, Z. Li, B. Deng, C. Ye, L. Zhang, Y. Wang, T. Li, Q. Liu, G. Cui, A.M. Asiri, Y. Luo, X. Sun, Superior hydrogen evolution electrocatalysis enabled by CoP nanowire array on graphite felt, *Int. J. Hydrog. Energy* 47 (2022) 3580–3586, <https://doi.org/10.1016/j.ijhydene.2021.11.039>.
- [20] X. Yu, S. Zhang, C. Li, C. Zhu, Y. Chen, P. Gao, L. Qi, X. Zhang, Hollow CoP nanoparticle/N-doped graphene hybrids as highly active and stable bifunctional catalysts for full water splitting, *Nanoscale* 8 (2016) 10902–10907, <https://doi.org/10.1039/c6nr01867j>.
- [21] X. Wei, Y. Zhang, H. He, L. Peng, S. Xiao, S. Yao, P. Xiao, Carbon-incorporated porous honeycomb NiCoFe phosphide nanospheres derived from a MOF precursor for overall water splitting, *Chem. Comm.* 55 (2019) 10896–10899, <https://doi.org/10.1039/c9cc05225a>.
- [22] T.L. Luyen Doan, D.T. Tran, D.C. Nguyen, H. Tuan Le, N.H. Kim, J.H. Lee, Hierarchical three-dimensional interface assembled from oxygen-doped cobalt phosphide layer-shelled metal nanowires for efficient electrocatalytic water splitting, *Appl. Catal. B Environ.* 261 (2020) 118268–118281, <https://doi.org/10.1016/j.apcatb.2019.118268>.
- [23] E. Cao, Z. Chen, H. Wu, P. Yu, Y. Wang, F. Xiao, S. Chen, S. Du, Y. Xie, Y. Wu, Z. Ren, Boron-induced electronic-structure reformation of CoP nanoparticles drives enhanced pH-universal hydrogen evolution, *Angew. Chem. Int. Ed.* 59 (2020) 4154–4160, <https://doi.org/10.1002/anie.201915254>.
- [24] S. Xu, H. Zhao, T. Li, J. Liang, S. Lu, G. Chen, S. Gao, A.M. Asiri, Q. Wu, X. Sun, Iron-based phosphides as electrocatalysts for the hydrogen evolution reaction: recent advances and future prospects, *J. Mater. Chem. A* 8 (2020) 19729–19745, <https://doi.org/10.1039/d0ta05628f>.
- [25] B. Zhang, F. Yang, X. Liu, N. Wu, S. Che, Y. Li, Phosphorus doped nickel-molybdenum aerogel for efficient overall water splitting, *Appl. Catal. B Environ.* 298 (2021) 120494–120504, <https://doi.org/10.1016/j.apcatb.2021.120494>.
- [26] D. Chen, R.H. Lu, Z.H. Pu, J.W. Zhu, H.W. Li, F. Liu, S. Hu, X. Luo, J.S. Wu, Y. Zhao, S.C. Mu, Ru-doped 3D flower-like bimetallic phosphide with a climbing effect on overall water splitting, *Appl. Catal. B Environ.* 279 (2020) 119396–119404, <https://doi.org/10.1016/j.apcatb.2020.119396>.
- [27] Q. Hu, Z. Wang, X. Huang, Y. Qin, H. Yang, X. Ren, Q. Zhang, J. Liu, M. Shao, C. He, Integrating well-controlled core-shell structures into “superaerophobic” electrodes for water oxidation at large current densities, *Appl. Catal. B Environ.* 286 (2021) 119920–119928, <https://doi.org/10.1016/j.apcatb.2021.119920>.
- [28] S.Q. Wang, Y.L. Cao, W. Jia, Z.J. Lu, D.Z. Jia, A cage-confinement strategy to fabricate Pt-Mo₆Co₆C heterojunction for highly efficient PH-universal hydrogen evolution, *Appl. Catal. B Environ.* 298 (2021) 120579–120590, <https://doi.org/10.1016/j.apcatb.2021.120579>.
- [29] R. Xiang, Y. Duan, L. Peng, Y. Wang, C. Tong, L. Zhang, Z.D. Wei, Three-dimensional Core@Shell Co@CoMoO₄ nanowire arrays as efficient alkaline hydrogen evolution electro-catalysts, *Appl. Catal. B Environ.* 246 (2019) 41–49, <https://doi.org/10.1016/j.apcatb.2019.01.035>.
- [30] P. Ding, C. Meng, J. Liang, T. Li, Y. Wang, Q. Liu, Y. Luo, G. Cui, A.M. Asiri, S. Lu, X. Sun, NiFe layered-double-hydroxide nanosheet arrays on graphite felt: a 3D electrocatalyst for highly efficient water oxidation in alkaline media, *Inorg. Chem.* 60 (2021) 12703–12708, <https://doi.org/10.1021/acs.inorgchem.1c01783>.
- [31] C. Guan, W. Xiao, H.J. Wu, X.M. Liu, W.J. Zang, H. Zhang, J. Ding, Y.P. Feng, S. J. Pennycook, J. Wang, Hollow Mo-doped CoP nanoarrays for efficient overall water splitting, *Nano Energy* 48 (2018) 73–80, <https://doi.org/10.1016/j.nanoen.2018.03.034>.
- [32] F. Li, G.F. Han, H.J. Noh, Y.L. Lu, J. Xu, Y.F. Bu, Z.P. Fu, J.B. Baek, Construction of porous Mo₃P/Mo nanobelts as catalysts for efficient water splitting, *Angew. Chem. Int. Ed.* 57 (2018) 14139–14143, <https://doi.org/10.1002/anie.201808844>.
- [33] L.M. Cao, Y.W. Hu, S.F. Tang, A. Iljin, J.W. Wang, Z.M. Zhang, T.B. Lu, Fe-CoP electrocatalyst derived from a bimetallic prussian blue analogue for large-current-density oxygen evolution and overall water splitting, *Adv. Sci.* 5 (2018) 1800949–1800958, <https://doi.org/10.1002/advs.201800949>.
- [34] Y. Sun, X. Wang, A. Li, X. Zheng, L. Peng, J. Huang, Z. Deng, H. Chen, Z.D. Wei, Rational construction of macroporous CoFeP triangular plate arrays from bimetal–organic frameworks as high-performance overall water-splitting catalysts, *J. Mater. Chem. A* 7 (2019) 17529–17535, <https://doi.org/10.1039/c9ta05282h>.
- [35] H. Li, Q. Li, P. Wen, T.B. Williams, S. Adhikari, C. Dun, C. Lu, D. Itanze, L. Jiang, D. L. Carroll, G.L. Donati, P.M. Lundin, Y. Qiu, S.M. Geyer, Colloidal cobalt phosphide nanocrystals as trifunctional electrocatalysts for overall water splitting powered by a zinc-air battery, *Adv. Mater.* 30 (2018) 1705796–1705804, <https://doi.org/10.1002/adma.201705796>.
- [36] Y. Sun, S. Xu, C.A. Ortiz-Ledón, J. Zhu, S. Chen, J. Duan, Biomimetic assembly to superplastic metal–organic framework aerogels for hydrogen evolution from seawater electrolysis, *Exploration* 1 (2021) 20210021–20210029, <https://doi.org/10.1002/exp.20210021>.
- [37] S.L. Zhao, Y. Wang, J.C. Dong, C.T. He, H.J. Yin, P.F. An, K. Zhao, X.F. Zhang, C. Gao, L.J. Zhang, J.W. Lv, J.X. Wang, J.Q. Zhang, A.M. Khattak, N.A. Khan, Z. X. Wei, J. Zhang, S.Q. Liu, H.J. Zhao, Z.Y. Tang, Ultrathin metal-organic framework nanosheets for electrocatalytic oxygen evolution, *Nat. Energy* 1 (2016) 1–10, <https://doi.org/10.1038/Nenergy.2016.184>.
- [38] Y. Song, K. Ji, H. Duan, M. Shao, Hydrogen production coupled with water and organic oxidation based on layered double hydroxides, *Exploration* 1 (2021) 20210050–20210062, <https://doi.org/10.1002/exp.20210050>.
- [39] S. Rezaee, S. Shahrokhian, Facile synthesis of petal-like NiCo/NiO-CoO/nanoporous carbon composite based on mixed-metallic MOFs and their application for electrocatalytic oxidation of methanol, *Appl. Catal. B Environ.* 244 (2019) 802–813, <https://doi.org/10.1016/j.apcatb.2018.12.013>.
- [40] Z. Chen, B. Fei, M. Hou, X. Yan, M. Chen, H. Qing, R. Wu, Ultrathin Prussian blue analogue nanosheet arrays with open bimetal centers for efficient overall water splitting, *Nano Energy* 68 (2020) 104371–104381, <https://doi.org/10.1016/j.nanoen.2019.104371>.
- [41] Y.N. Guo, J. Tang, Z.L. Wang, Y. Sugahara, Y. Yamauchi, Hollow porous heterometallic phosphide nanocubes for enhanced electrochemical water splitting, *Small* 14 (2018) 1802442–1802450, <https://doi.org/10.1002/smll.201802442>.
- [42] H. Sun, X. Xu, Y. Song, W. Zhou, Z. Shao, Designing high-valence metal sites for electrochemical water splitting, *Adv. Funct. Mater.* 31 (2021) 2009779–2009823, <https://doi.org/10.1002/adfm.202009779>.
- [43] H. Zhang, P. Li, S. Chen, F. Xie, D.J. Riley, Anodic transformation of a core-shell prussian blue analogue to a bifunctional electrocatalyst for water splitting, *Adv. Funct. Mater.* 31 (2021) 2106835–2106847, <https://doi.org/10.1002/adfm.202106835>.
- [44] X. Zheng, B. Zhang, P. De Luna, Y. Liang, R. Comin, O. Voznyy, L. Han, F.P. Garcia de Arquer, M. Liu, C.T. Dinh, T. Regier, J.J. Dynes, S. He, H.L. Xin, H. Peng, D. Prendergast, X. Du, E.H. Sargent, Theory-driven design of high-valence metal sites for water oxidation confirmed using in situ soft X-ray absorption, *Nat. Chem.* 10 (2018) 149–154, <https://doi.org/10.1038/nchem.2886>.
- [45] H. Sun, X. Xu, Y. Song, W. Zhou, Z. Shao, Designing high-valence metal sites for electrochemical water splitting, *Adv. Funct. Mater.* 31 (2021) 2009779–2009823, <https://doi.org/10.1002/adfm.202009779>.
- [46] Z. Wang, P. Guo, S. Cao, H. Chen, S. Zhou, H. Liu, H. Wang, J. Zhang, S. Liu, S. Wei, D. Sun, X. Lu, Contemporaneous inverse manipulation of the valence configuration to preferred Co²⁺ and Ni³⁺ for enhanced overall water electrocatalysis, *Appl. Catal. B Environ.* 284 (2021) 119725–119825, <https://doi.org/10.1016/j.apcatb.2020.119725>.